Supplementary Material of

Sea ice leads in the Arctic Ocean: Model assessment, interannual variability and trends

Q. Wang, S. Danilov, T. Jung, L. Kaleschke, and A. Wernecke

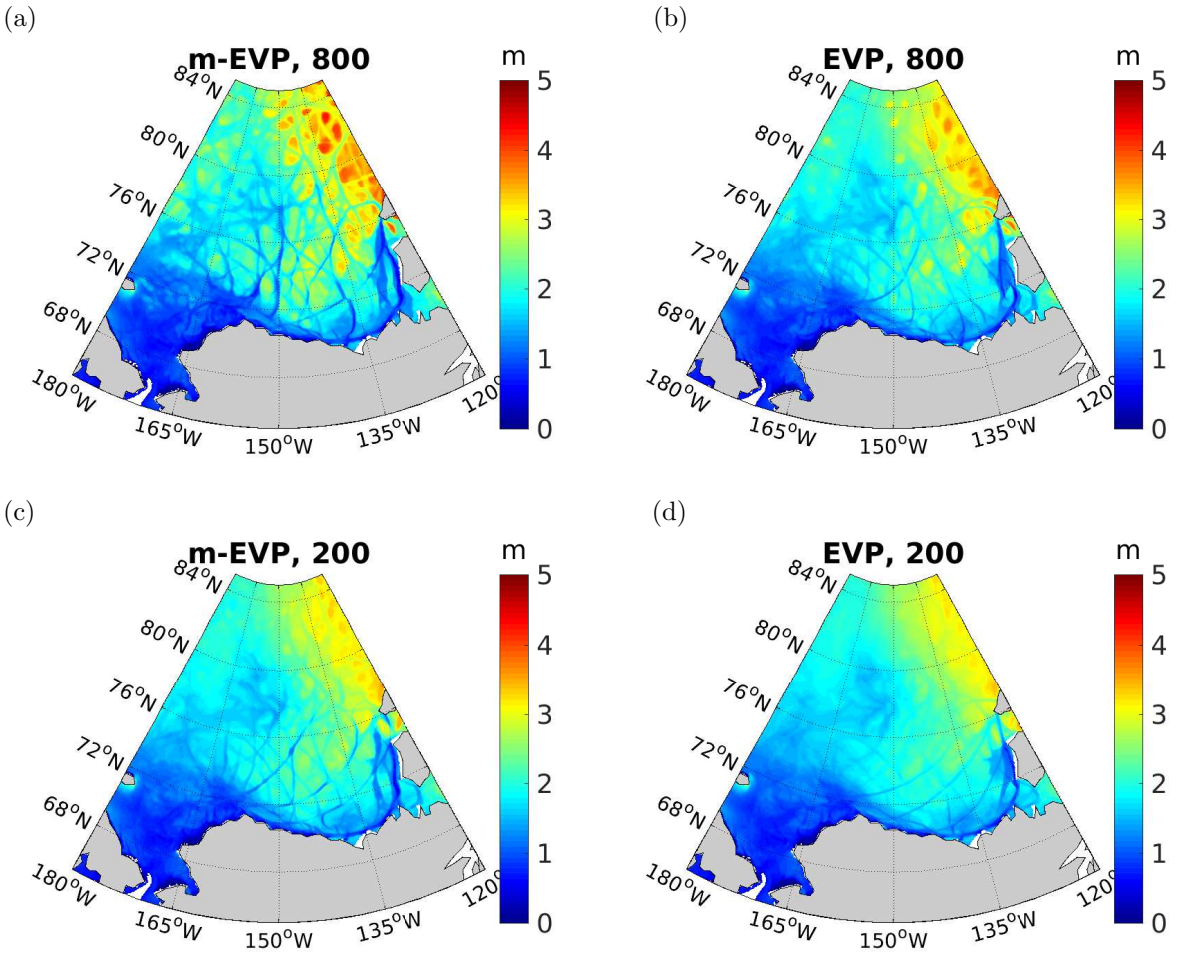

Supplementary Material, Figure S1: Sea ice thickness on 1 January 2004 simulated on the 4.5 km resolution mesh. The results are from four experiments that differ in the details of the sea ice rheology: (a) The updated version of EVP with 800 subcycling steps; this setting is used in the simulation analyzed in this paper. (b) The original EVP method with 800 subcycling steps. (c) The updated version of EVP with 200 subcycling steps. (d) The original EVP method with 200 subcycling steps. This figure and Fig. 1(c) illustrate the importance of converged solution in representing sea ice leads.

(a)

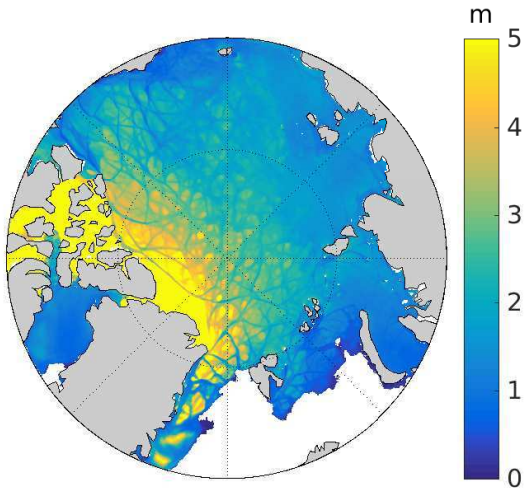

(b)

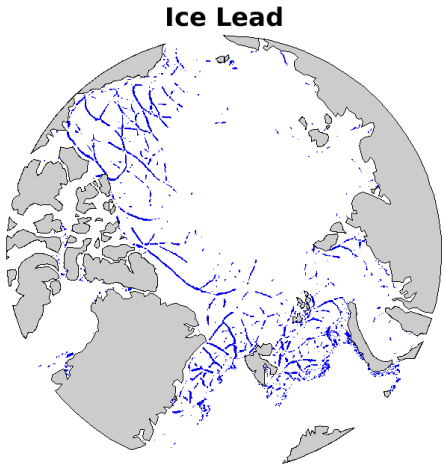

(c)

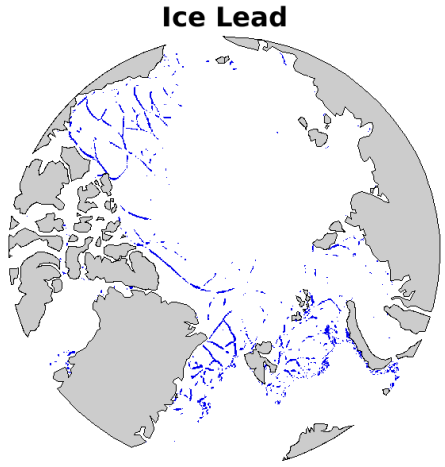

Supplementary Material, Figure S2: (a) Simulated sea ice thickness on 1 January 2004 with the horizontal resolution of 4.5 km. (b) The identified sea ice leads from the sea ice thickness field shown in (a). Leads are locations where sea ice is at least 20% thinner than at its surroundings; this is the definition used in the paper. (c) The same as (b) but with a 30% threshold. Most of the visually apparent cracks shown in (a) are well identified in (b), but not in (c).

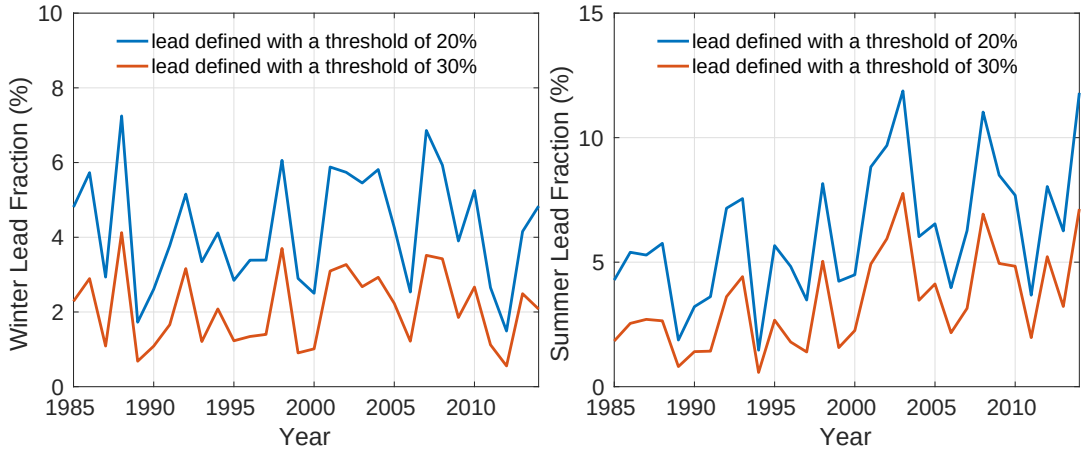

Supplementary Material, Figure S3: Time series of lead area fraction using two different thresholds for identifying ice leads: winter mean (JFM, left) and summer mean (JAS, right). The results with the two thresholds are highly correlated with each other ($r > 0.97$). Although the magnitude of the lead fraction is sensitive to the threshold used, the conclusion of this study regarding variability and trends of leads are not affected by the choice of the threshold. Because the threshold of 20% can better identify most of the visually apparent cracks (Fig. S2), we used this value in this study.

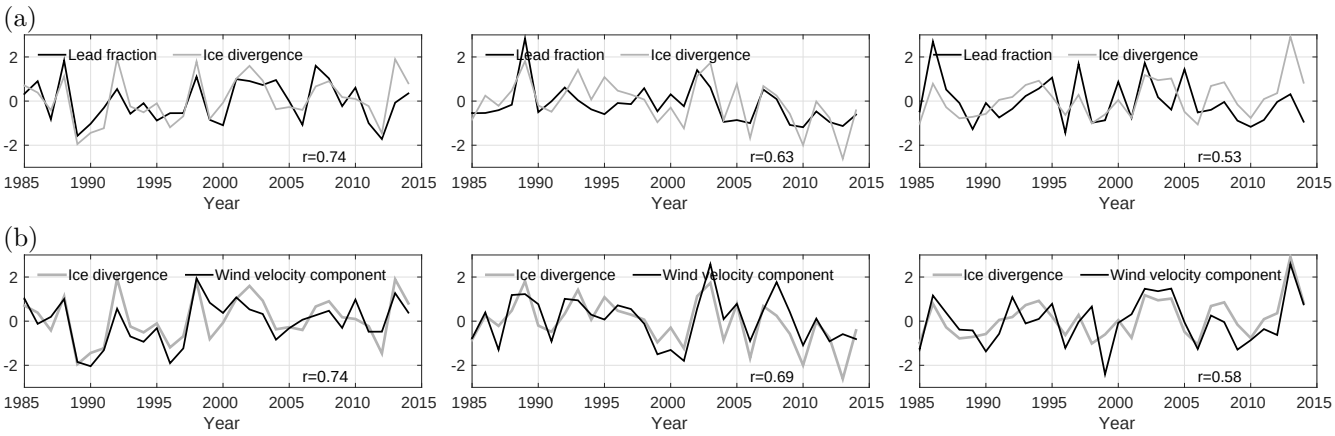

Supplementary Material, Figure S4: (a) Normalized time series of lead area fraction and sea ice divergence and (b) normalized time series of sea ice divergence and wind speed in winter (JFM). The three averaging regions from left to right are indicated in Fig. 4 with indices 1 to 3, respectively. The wind speed is shown for the component in the direction that has largest correlation with ice divergence. The directions for the three regions are 74° northwest, 12° northeast, and 40° northwest, respectively. The correlation coefficients are shown in the corresponding panels; all the correlations are significant at the 95% confidence level. Lead area fraction has no significant trend in winter.

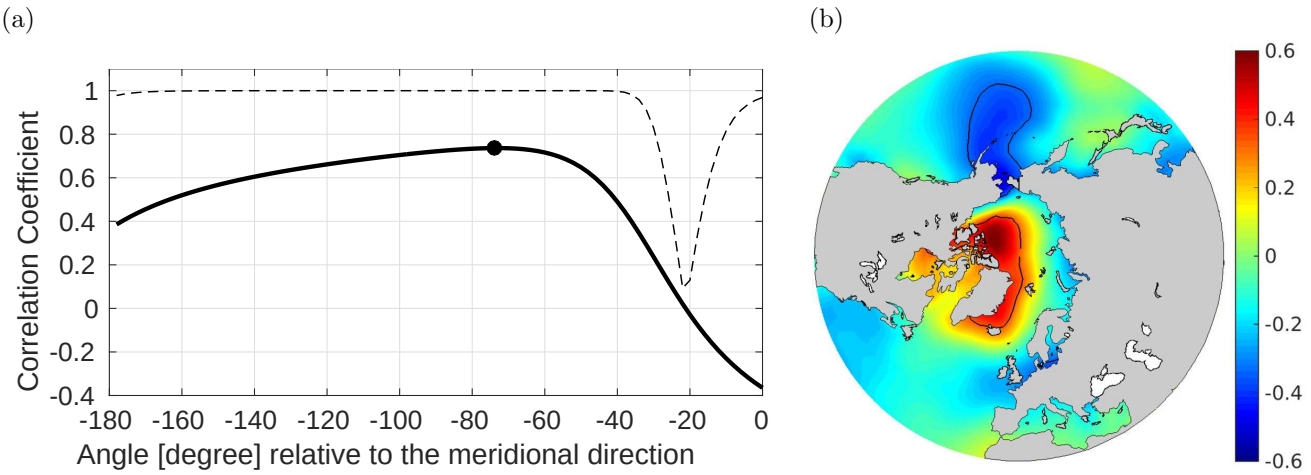

Supplementary Material, Figure S5: (a) Correlation coefficients between wintertime (JFM) sea ice divergence and wind velocity components at different direction for the Beaufort Sea (BS) region. The confidence level is shown by the dashed line. The location of maximal correlation coefficient is indicated by the black dot. (b) Correlation between BS sea ice divergence and the sea level pressure. The area of 95% confidence level is indicated with black contours.

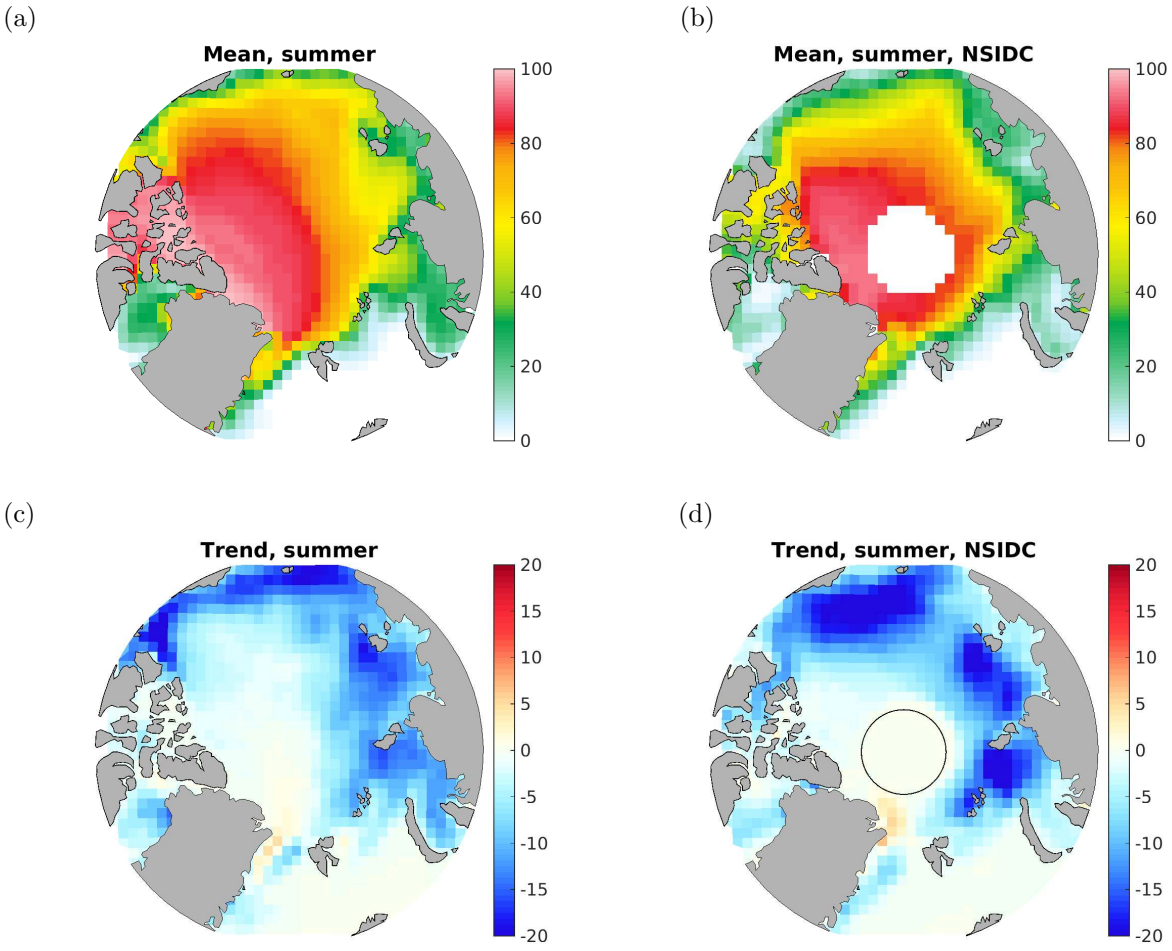

Supplementary Material, Figure S6: Simulated (a) and observed (b) summertime (JAS) mean sea ice concentration (%). Simulated (c) and observed (d) linear trend of summertime sea ice concentration (%/decade). The observation is based on the NSIDC data. The period of 1985–2014 is used in the analysis.

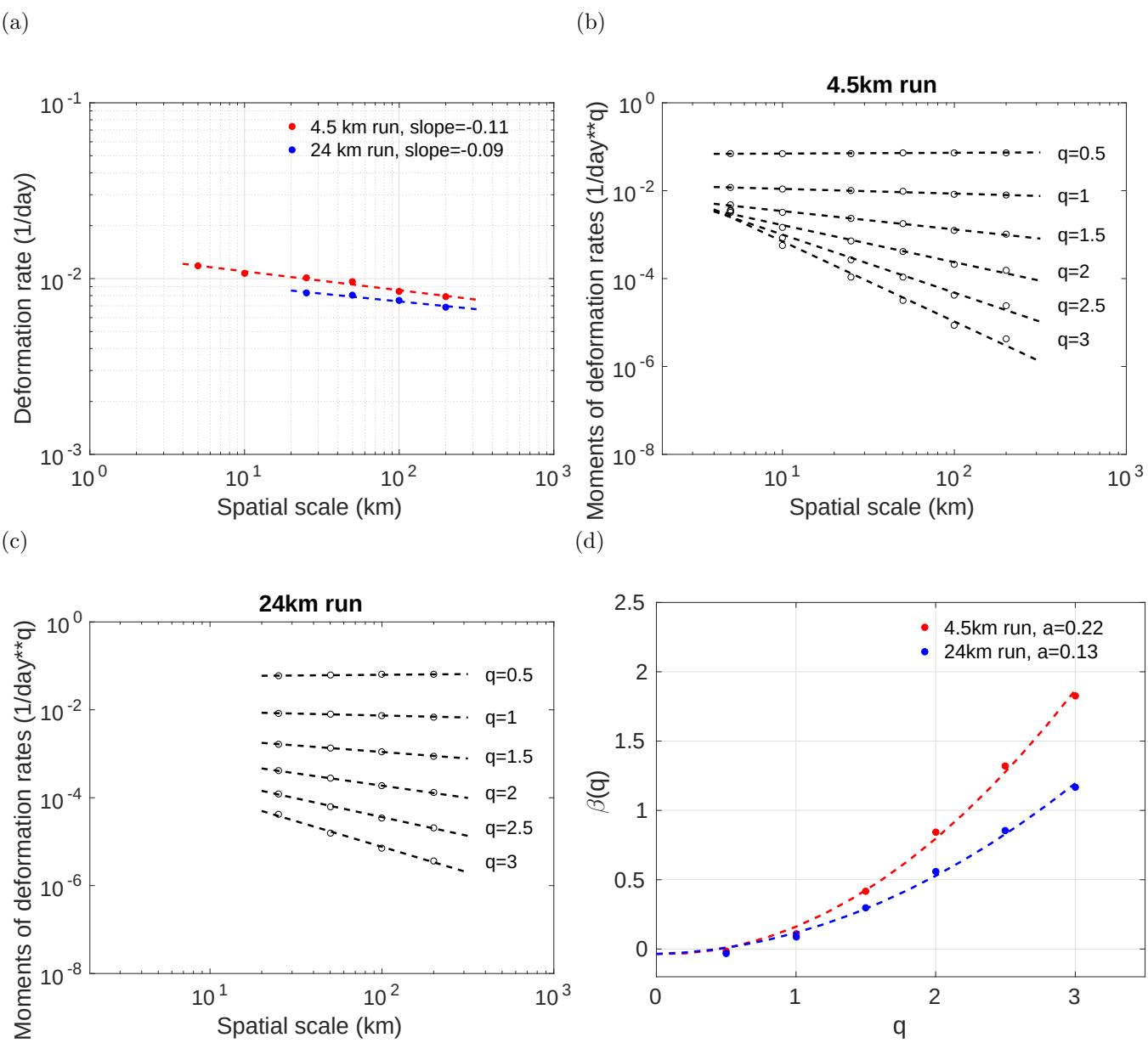

Supplementary Material, Figure S7: (a) Mean total deformation rate $\langle\dot{\epsilon}\rangle$ as a function of the spatial scale L for the two simulations at different horizontal resolutions. The dashed lines are the least squares fits for the two model results: $\langle\dot{\epsilon}\rangle \sim L^{-0.11}$ for the 4.5 km resolution simulation and $\langle\dot{\epsilon}\rangle \sim L^{-0.09}$ for the 24 km simulation. The exponents are the slopes of the dashed lines in the log-log plot. The coarse-graining is done until the 200 km scale, as coarser scales will lead to too few grid cells for analysis. The power-law exponent derived from observations by Bouillona and Rampal (2015b) is -0.12. (b) Moments of the total deformation rate $\langle\dot{\epsilon}^q\rangle$ as a function of the spatial scale L for $q = 0.5 - 3$ for the 4.5 km resolution simulation. Dashed lines are power-law fits for different moments ($\langle\dot{\epsilon}^q\rangle \sim L^{-\beta(q)}$). (c) The same as (b) but for the 24 km resolution simulation. (d) The slope $\beta(q)$ of the dashed lines in (b,c) are plotted as a function of the moment order q along with the best (in the least-square sense) quadratic fits $\beta(q) = aq^2 + bq$. The curvature a indicates the degree of multifractality. $a = 0.22$ and 0.13 in the 4.5 km and 24 km resolution simulations respectively. The analysis is done over the Canadian Basin, where RGPS winter data are mainly available; and the results are averaged over the winter months (JFM) of 2004. Reference: Bouillon, S. and Rampal, P. (2015b), On producing sea ice deformation data sets from SAR-derived sea ice motion, The Cryosphere, 9, 663-673.